



Bathymetric Control on Borchgrevink and Roi Baudouin Ice Shelves in East Antarctica

Hannes Eisermann¹ , Graeme Eagles¹ , Antonia Stefanie Ruppel² , Andreas Läufer², and Wilfried Jokat^{1,3} 

¹Alfred Wegener Institute for Polar and Marine Research, Bremerhaven, Germany, ²Federal Institute for Geosciences and Natural Resources, Hannover, Germany, ³University of Bremen, Bremen, Germany

Key Points:

- We have generated bathymetric models based on gravity inversion beneath the Roi Baudouin and Borchgrevink ice shelves
- Results are similar to ice shelves throughout the entire Dronning Maud Land, which are all crossed by deep troughs and bathymetric sills
- Deep gateways leading from the open ocean into ice shelf cavities possibly allow for the intrusion of Warm Deep Water into these cavities

Correspondence to:

H. Eisermann,
heiserma@awi.de

Citation:

Eisermann, H., Eagles, G., Ruppel, A. S., Läufer, A., & Jokat, W. (2021). Bathymetric control on Borchgrevink and Roi Baudouin ice shelves in East Antarctica. *Journal of Geophysical Research: Earth Surface*, 126, e2021JF006342. <https://doi.org/10.1029/2021JF006342>

Received 6 JUL 2021
Accepted 15 SEP 2021

Abstract The stability of ice shelves and drainage of ice sheets they buttress is largely determined by melting at their atmospheric and oceanic interfaces. Subglacial bathymetry can impact ice shelf stability because it influences the onset and the pattern of warm ocean water incursions into the cavities between them and the seafloor. Bathymetry is further important at pinning points, which significantly retard the flow of ice shelves. This effect can be lost instantaneously if basal and surface melting cause an ice sheet to thin and lift off its pinning points. With all this in mind, we have developed a model of bathymetry beneath the western Roi Baudouin and central and eastern Borchgrevink ice shelves in Dronning Maud Land based on inversion from gravity data and tied to available depth references offshore and subglacial topography inland of the grounding line. The model shows deep glacial troughs beneath the ice shelves and bathymetric sills close to the continental shelf. The central Borchgrevink Ice Shelf overhangs the continental slope by around 50 km, exposing its northern parts to the open ocean and higher ocean temperatures. Continuous troughs traverse the central Borchgrevink and western Roi Baudouin ice shelves at depths greater than the offshore thermocline and thus present a risk of Warm Deep Water intrusions into their cavities under the current and future oceanographic regimes. Differing bathymetric characteristics might explain the ice shelves' contrasting dominant mass loss processes.

Plain Language Summary The rate at which Antarctica's ice sheets flow off the continent is largely stabilized by floating ice shelves that form where they meet the surrounding ocean. Assessing the stability of this interconnected system strongly depends on correctly quantifying ice gain processes, such as snowfall, and ice mass loss processes, such as melting at the bases of the ice shelves. This basal melting strongly depends on the flow of warm ocean water into the cavity between the ice shelf and the seafloor below, which is in turn influenced by the shape of the seabed. Using sparse direct measurements together with small variations in the pull of gravity measured from airplanes, we have generated a model of the formerly unknown topography beneath the Borchgrevink and Roi Baudouin ice shelves in East Antarctica. The modeled seabed shows deep troughs beneath the ice shelves and topographic sills along the continental shelf. Gateways within these sills potentially allow for the intrusion of warm water into the cavities, representing a threat to future ice shelf stability.

1. Introduction

Ice shelves play a major role in maintaining the stability of their respective ice sheets (e.g., Haseloff & Sergienko, 2018; Gudmundsson et al., 2019). If an ice shelf loses mass, the loss is balanced by an increased drainage of its linked ice sheet (Dupont & Alley, 2005). Without compensating mass gain processes such as snowfall or basal accretion, the system as a whole suffers net mass loss and contributes to global sea-level rise. The balance can be forced toward mass loss by both atmospheric and oceanographic processes that deliver oceanic heat to ice shelf bases, which duly melt (Depoorter et al., 2013; Rignot et al., 2013). Knowledge of the bathymetry beneath the ice shelves has been shown to be crucial for estimating these basal melt rates (Goldberg et al., 2019; Tinto et al., 2015). Bathymetric features can be the deciding factor for whether, and in what quantity, warm water masses breach into the water cavities beneath the ice shelves. A good understanding of subglacial bathymetry is therefore necessary for an improved knowledge of future ice shelf and ice sheet stability.

© 2021. The Authors.

This is an open access article under the terms of the [Creative Commons Attribution License](https://creativecommons.org/licenses/by/4.0/), which permits use, distribution and reproduction in any medium, provided the original work is properly cited.

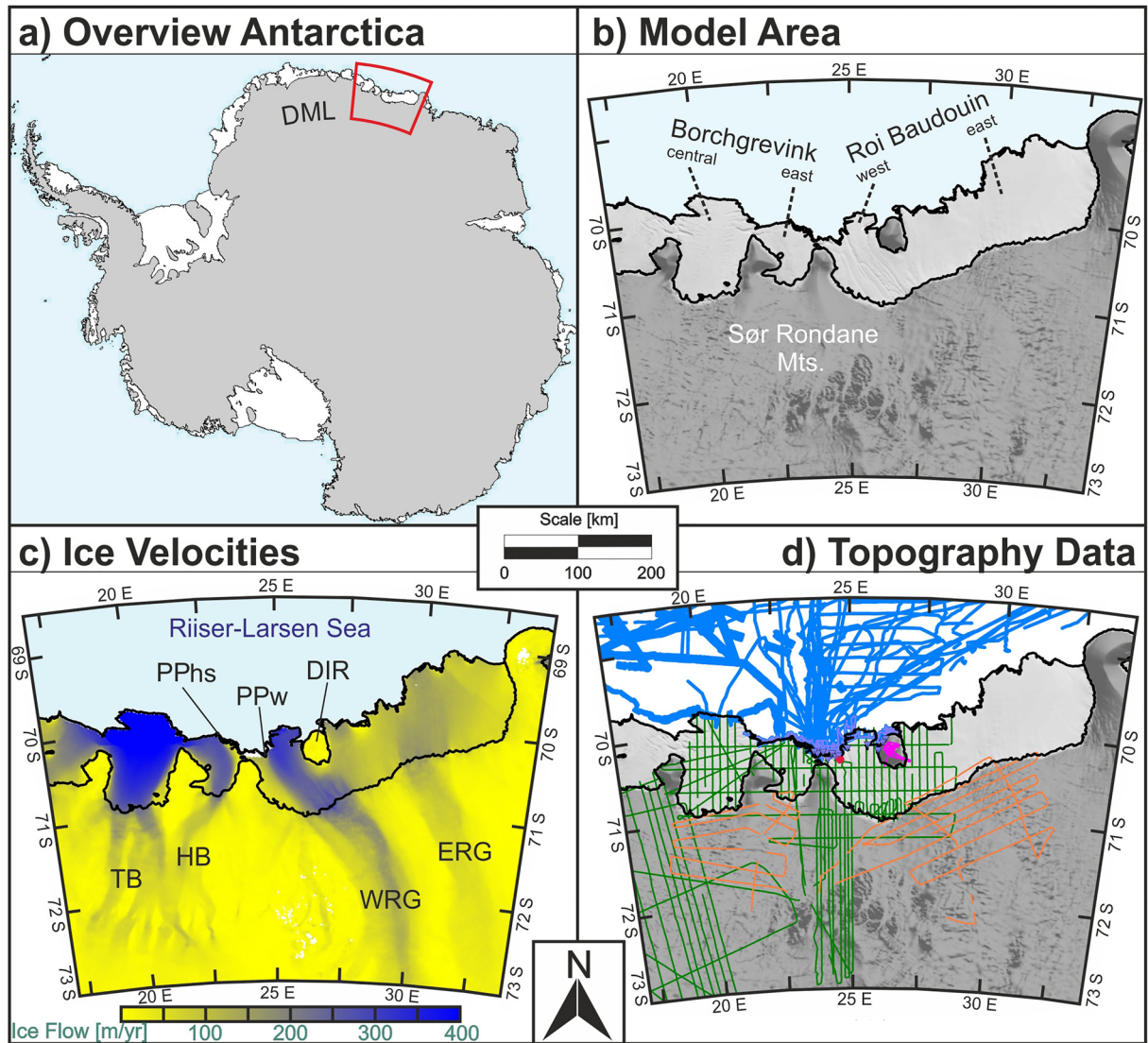


Figure 1. Ice shelves of eastern DML in East Antarctica. The overview in (a) is depicted with grounded ice in gray and ice shelves in white and open ocean in light blue. The RBIS and BIS in (b), north of the Sør Rondane Mountains, are overlain by the digital elevation model of Howat et al. (2019). The ice shelves are fed by the Tussebreen (TB) and Hansenbreen (HB), and the West Ragnhild (WRG) and East Ragnhild (ERG) glaciers shown in (c) with regions of main ice flow (Mouginot et al., 2017b). Prominent features along the calving front are the Derwael Ice Rise (DIR) and two pinning points (PPhs and PPw). Available topographic data (d) derived from radar data acquired during GEA campaigns (green), radar data by Callens et al. (2015, orange), and Drews (2019a, pink). Offshore, swath bathymetry data stem from multibeam (Schenke et al., 2010; Voß et al., 2011, blue), single-beam (NOAA database, also blue), and from hydroacoustic data and CTD casts by the Université libre de Bruxelles (Derwael, 1985; Favier et al., 2016; Berger, 2017; F. Pattyn, pers. comm.; all purple). Additional data for PPw stems from satellite observations by Drews (2019b, red point). Grounding lines and calving fronts for all panels are extracted from Mouginot et al. (2017a). The scale is valid for (b), (c), and (d).

Measurements of sub-ice-shelf seafloor depth are sparse because of the logistical challenges to acquire seismic and bathymetric data across and below ice shelves. The Roi Baudouin (RBIS) and Borchgrevink (BIS) ice shelves in eastern Dronning Maud Land (DML, Figure 1) are no exception; in fact, no subice bathymetry data exist for either. Existing topographic compilations (Fretwell et al., 2013; Morlighem et al., 2020) portray them with depth estimates that are derived by long-distance interpolations between radar-derived bedrock elevations inland of the grounding lines and hydroacoustic data off the ice shelves.

A cost-effective method to generate a more reliable estimate of the subice bathymetry is an inversion of airborne gravity data. Gravity data reflect the subsurface mass distribution related to density contrasts between bodies of ice, water, and bedrock and so can be used to model the shapes of their interfaces. In this study, we

describe the generation of bathymetric models in this way, supported by reference points from single- and multibeam hydroacoustic data along the calving fronts and ice-penetrating radar data in grounded areas. We interpret the updated model in terms of the glacial history as well as the present and future stability of the BIS, RBIS, and their related ice sheets.

1.1. Research Area

The RBIS and BIS lie along the Ragnhild Coast from about 19°E to 33°E in eastern DML (Figure 1). Geologically, the area was shaped by the amalgamation and breakup of Gondwana. Two models aim to explain the final amalgamation process whereof one proposes a continuation of the East African Orogen into DML, the East African-Antarctic Orogen (Jacobs & Thomas, 2004). A second model introduces the E-W-trending Kunga Orogen (Meert et al., 1995) in which large parts of DML constitute a mega-nappe rooting in northern Mozambique (e.g., Grantham et al., 2003; Meert, 2003). New geological findings refine the first model and indicate a rather complex tectonic history for eastern DML with repeated phases of accretion, magmatism, and reactivation (e.g., Elburg et al., 2016; Jacobs et al., 2015; Ruppel et al., 2020). The breakup saw the development of large volumes of magma that were intruded into the later continental shelf, as observable in seismic reflection (Leitchenkov et al., 2008) and magnetic data (Golynsky et al., 1996; Mieth et al., 2014; Müller & Jokat, 2019).

The ice shelves lie north of the Sør Rondane Mountains, which are part of the DML mountain chain. This mountain chain ends seaward at a tall escarpment, the product of post-breakup erosional backwearing and downwearing. Over and inland of the mountains, the drainage system developed from a period of alpine style glaciation is still preserved beneath the ice and only slightly overprinted by later ice-sheet processes (Eagles et al., 2018; Franke et al., 2021; Näslund, 2001).

The RBIS, with an area of almost 33,000 km², comprises western and eastern parts, separated by the Derwael Ice Rise, which are fed by the West Ragnhild Glacier and East Ragnhild Glacier (Figure 1). The West Ragnhild Glacier is one of the three largest outlet glaciers in DML, besides the Jutulstraumen and the Shirase Glacier, accounting for about 10% of DML's total ice discharge (Callens et al., 2014; Rignot et al., 2013). Two shorter glaciers, the Tussebreen and Hansenbreen, drain into the BIS, which spans an area of 21,500 km². Together, the RBIS and BIS drain a catchment of almost 500,000 km², with 747,961 Gt of ice above the sea level (according to Bedmap2; Fretwell et al., 2013), equivalent to 2.07 m of eustatic sea-level rise. The beds of all the glaciers lie mostly below the sea level (Callens et al., 2014) and dip southward toward the ice sheet interior, leaving them potentially unstable and vulnerable to ocean forcing (Favier et al., 2016; Gudmundsson et al., 2012). While the two ice shelves experience comparable absolute mass losses, the majority of ice from the RBIS is lost by basal melting, whereas BIS mass loss is dominated by calving events (Rignot et al., 2013).

Knowledge of ice rises and promontories beneath the ice shelves is key for reliable assessment of their future stability, because they retard grounding line retreat while grounded ice remains pinned on them (Berger et al., 2016; Favier et al., 2012). Favier et al. (2016) present two pinning points along the calving fronts of the eastern BIS, named PPhs, and the western RBIS, named PPw (Figure 1c).

Despite significant historical calving events (Nishio et al., 1984), the RBIS appears to be in a steady-state on a millennial timescale (Berger et al., 2016; Drews et al., 2015; Favier & Pattyn, 2015), without noticeable changes of the grounding line position in recent decades (Drews et al., 2017). Ice-sheet modeling using the present, essentially unknown, bathymetry predicts a stable RBIS in the future (Favier et al., 2016). A trough beneath the western RBIS, inferred by Favier et al. (2016) to coincide with the modern-day ice flow path, is the main point of potential vulnerability.

The narrow continental shelf off eastern DML in the Riiser-Larsen Sea (Figure 1c) permits a strong interaction between a westward coastal current and water within the cavities beneath the ice shelves. The coastal current mostly consists of cold and fresh Eastern Shelf Water (ESW; Nicholls et al., 2009) and Warm Deep Water (WDW; Carmack & Foster, 1975) separated by the Antarctic Slope Front. The cold-cavity ice shelves of DML (Rignot et al., 2013) accommodate ESW, which mostly blocks out the warmer and saltier WDW (Nicholls et al., 2009). A small amount of WDW has been shown to intrude the Fimbul Ice Shelf cavity (Hattermann et al., 2014) to the west of our study area. The RBIS may suffer similar intrusions, depending

on the geometry of the trough inferred by Favier et al. (2016). One general feature of a narrow continental shelf in combination with easterly winds is the seasonal intrusion of solar-heated Antarctic Surface Water (ASW) during sea ice-free periods (Zhou et al., 2014). Based on the regional bathymetry and the assumed blockage of WDW, basal melt rates for the RBIS seem to be predominantly caused by ASW intrusion and tide-related topographic waves (Sun et al., 2019).

Compared with the RBIS, virtually nothing is known in detail about the BIS. Although understandable in terms of the volume flux of their feeder glaciers, this disparity is more problematic to the understanding of the region. While its area is just two thirds that of the RBIS, the BIS currently suffers slightly greater rates of absolute ice mass loss (Rignot et al., 2013).

2. Materials and Methods

2.1. Surveys and Auxiliary Data

The bathymetric model presented here is mainly based on geophysical data sets acquired over the course of three consecutive seasons in early 2011, early 2012, and late 2012 using the Alfred Wegener Institute's Basler BT-67 aircrafts "Polar 5" and "Polar 6." The data were acquired within the research program "Geodynamic Evolution of East Antarctica" (GEA I–GEA III), a cooperative project between the Alfred Wegener Institute and the Federal Institute for Geosciences and Natural Resources. Gravity, magnetic, and radio echo sounding data were simultaneously acquired with line spacings of 5–10 km.

The GEA gravity data (with flight lines depicted in Figure 2a) are inverted for bathymetry, while ice-penetrating radar data (Figures 1d and 2b) provide the ice thicknesses that constrain the bathymetry modeling. The GEA magnetic data are published in Mieth et al. (2014) and Ruppel et al. (2018). Depth references for the model area are extracted from GEA and additional non-GEA radar data (Callens et al., 2015; Drews, 2019a) in grounded areas, from CTD casts and satellite-inferred depths close to the calving front (Drews, 2019b; Favier et al., 2016) and from shipborne single- and multibeam hydroacoustic data offshore (Figure 1d; Derwael, 1985; Favier et al., 2016; Schenke et al., 2010; Voß et al., 2011). A full list of data sources and survey ID's is given in the data supplement (see Data Availability).

2.2. Gravity Data

Gravity data were acquired with the ZLS Ultrasys modified LaCoste & Romberg Air/Sea gravimeter (S/N 56) mounted on a gimbal-stabilized platform close to the airplanes' centers of gravity at a sampling rate of 1 Hz. The navigation data, necessary for deriving gravity anomalies from the accelerations recorded by the gravimeter, are processed using precise point positioning. Flight segments involving turns, climbs and descents were discarded because the retrieval of reliable gravity data with Air/Sea meters depends on data acquisition during straight and level flight. The measured gravity anomaly data are corrected for tidal and geographical influences as well as instrument drift and station height to gain the free air anomaly (Figure 2c). A time-domain filter of 90 s applied to data collected at a flight speed of 70 m/s results in a spatial resolution of 6.3 km (Riedel et al., 2012). A crossover analysis after a statistical-leveling process yields a set of cross-point errors with a standard deviation of 5.8 mGal.

2.3. Radio Echo Sounding Data

The ice-penetrating radar we used operates with a 150-MHz signal generated by a synthesizer with burst durations of 60 or 600 ns and uses two short backfire antennas, one mounted underneath each aircraft wing (Nixdorf et al., 1999). The radar suffered from low penetration during one of the three campaigns, owing to a faulty design component, and only delivered ice thicknesses across the ice shelves (Figure 1). Therefore, the data set is complemented by auxiliary data (Figure 1d). Ice thicknesses from the GEA campaigns are determined with an average radar wave propagation speed in ice of $1.68 \cdot 10^8$ m/s. A firn correction is applied to account for higher velocities within the upper layer of the ice sheet (Blindow, 1994). An error estimate of ± 20 m is defined to account for errors in picking reflectors and inaccuracies of 0.5% concerning the propagation speed. The auxiliary data set of Callens et al. (2015) was acquired and processed with the

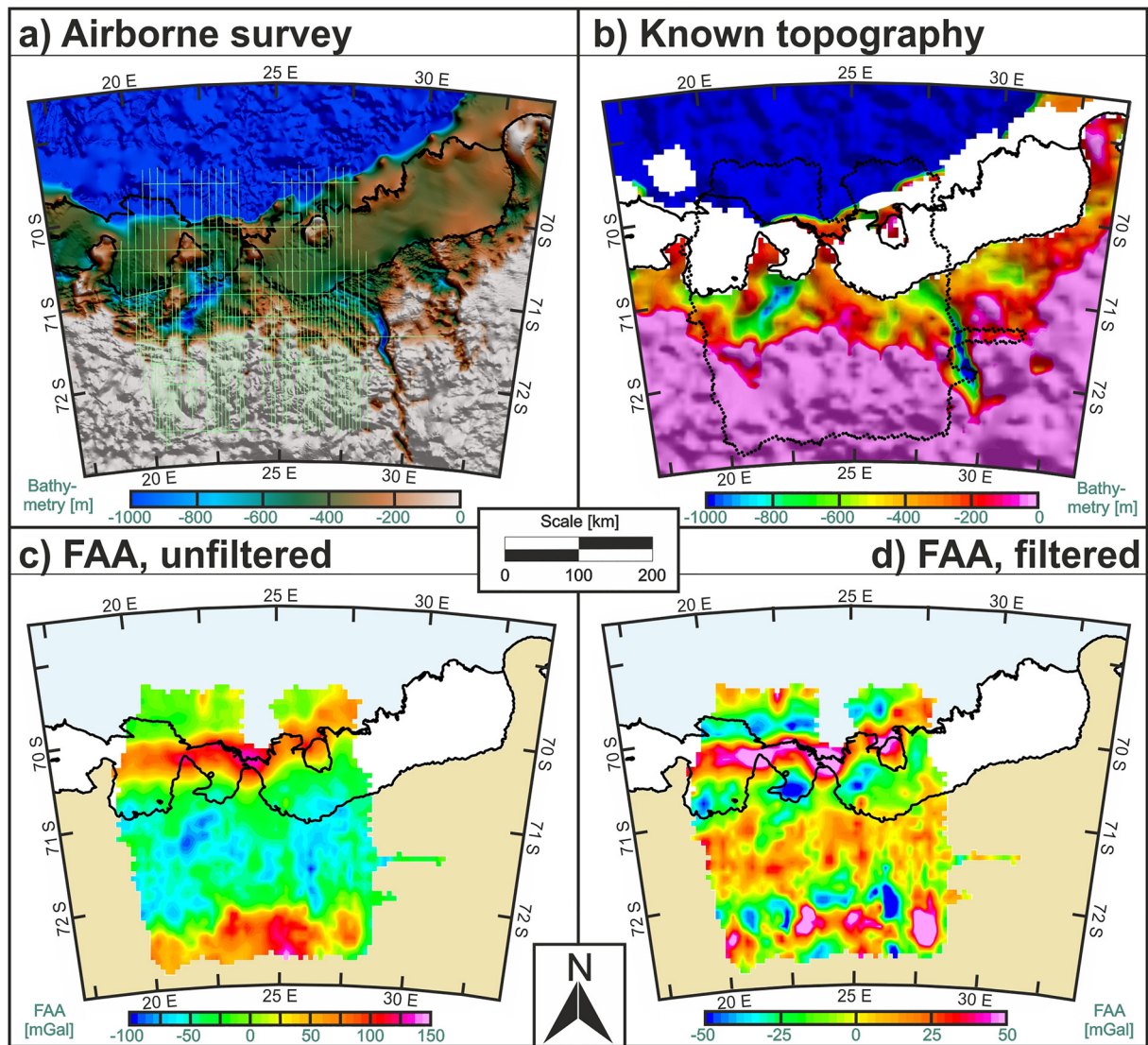


Figure 2. GEA I-III surveys. Airborne gravity data along flight lines (a) are used to develop bathymetric models in the areas of the unknown bathymetry beneath the RBIS and BIS in (b). The unfiltered free air anomaly (FAA) in (c) is filtered to achieve a mid-wavelength resemblance (d) to the known prevalent topography within the extent of the gravity grid in (b, dotted black line). The current topography model in (a) is extracted from Morlighem (2020), while grounding lines and ice shelf extents in all panels are inferred from Mougint et al. (2017a). The scale is valid for all panels.

same system and workflow as the GEA data. Calculated and extracted ice thicknesses are subtracted from the Reference Elevation Model of Antarctica (Howat et al., 2019) to determine the ice bottom elevation.

2.4. Bathymetric Modeling

Using the acquired geophysical data sets, we are able to produce topographic models of the seafloor underlying the RBIS and BIS. These bathymetric models are based on the inversion of gravity data under the constraints of sparse existing depth references at and beyond the grounding lines and calving fronts. We take a 3-D modeling approach based on the formulas of Parker (1973), as implemented within the *GM-SYS 3D* module of *Geosoft Oasis montaj*.

In a first step, we filter the gravity data in order to produce a gravity anomaly grid whose mid-wavelength variability resembles that of mid-wavelength bathymetric patterns inferred from the existing depth data. In the following section, we describe in detail how this step was designed to suppress the signals of large-scale

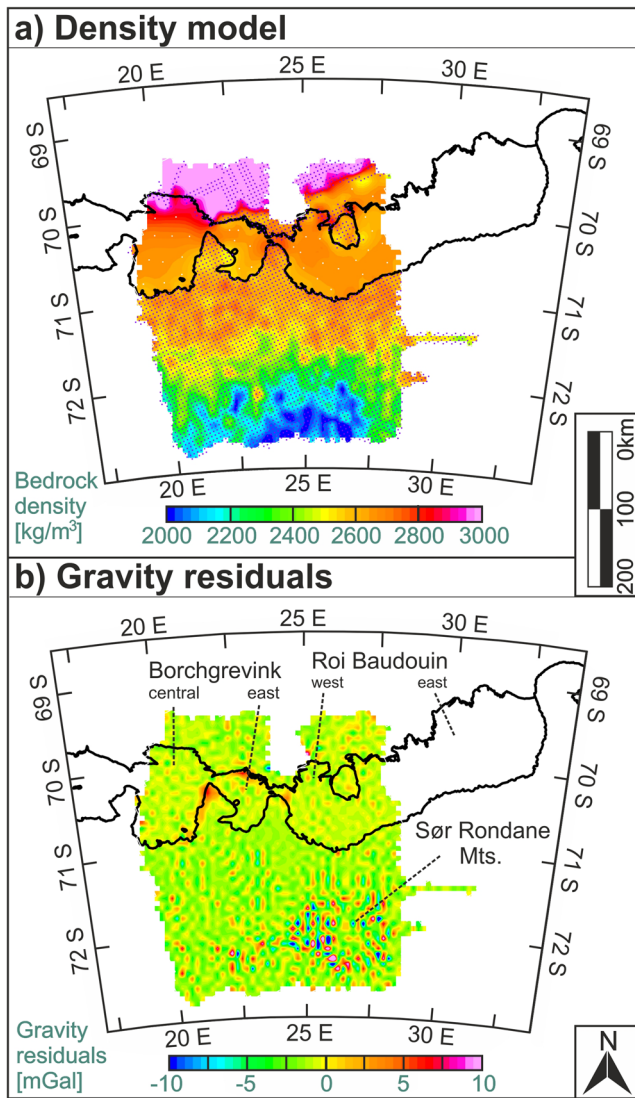


Figure 3. Bathymetric model generation. Density model generated during bathymetric modeling (a) with densities derived at known depth references (purple circles) and complemented densities at points of unknown depth (white circles). The population of gravity residuals after bathymetric modeling (b) shows a standard deviation of 4.5 mGal in the areas of unknown bathymetry beneath the ice shelves. The strongly undulating gravity residuals south of the western RBIS are related to the difficulty of modeling high topographic and bedrock density gradients in the geologically complex Sør Rondane Mountains.

geological processes and features related to crustal thinning near the continental margin. Our study area is situated at an extended continental margin, at which we can expect large (>100 km) topographic loads to be held in local isostatic equilibrium and so not to raise significant long-wavelength gravity signals (Watts & Moore, 2017). With this in mind, but to eliminate any remaining signals from subcrustal sources, we applied an isotropic band-pass filter cutting wavelengths longer than 150 km as well as those shorter than 5 km that are likely to be artifacts of aircraft motion or interpolation. Having eliminated the effects of very deep sources, we restricted the model domain depth to a maximum of 10 km.

Ice and water are assigned constant densities of 915 and 1030 kg/m³, respectively, and bedrock a starting value of 2,670 kg/m³. A DC shift of −1065 mGal was applied to the available gravity data set to align the starting model with the densely observed ice/bedrock interface inland of the grounding line and the observed water/bedrock interface beyond the calving front. This DC shift is set by implementing the average shift between the modeled and observed gravity data in areas directly encircling the ice shelves to get a good average for the area of unknown bathymetry beneath the ice shelves.

To account for medium-wavelength gravity signals of local isostatic compensation and laterally variable densities in the uppermost 10 km of the crust, we first invert for apparent bedrock densities and then extract the best-constrained model densities at locations where the bedrock elevation is known (Figure 3a, purple circles). On the ice shelves, large distances exist between such constrained points, over which we can expect significant geological variability to occur. To account for this, our density model is complemented by a linear interpolation between constrained points around the ice shelf margins (Figure 3a, white circles). The complemented density model was then used to invert for subglacial bathymetries. Within this inversion, the points of known depth were allowed to move slightly (maximum of ±30 m) to avoid the development of significant gravity residuals at these constraints.

The range of densities and their general oceanward increase, both shown in Figures 3a, is appropriate for the upper crustal geology of a glaciated extended continental margin. In detail, however, it seems clear that some residual local isostatic signal has also been accounted for. For example, the anomalously low densities coinciding with the Sør Rondane Mountains in the south of our model, where relatively dense igneous and metamorphic lithologies might be expected in the modeled upper 10 km of the crust, may reflect the density inversion's response to the presence of low-density rocks in the mountains' crustal root. As a result, the detailed pattern of densities is not reliably interpretable in terms of near-surface geological variability.

2.5. Gravity Anomalies Along the Extended Continental Margin of the Riiser-Larsen Sea

It is in the nature of potential field modeling that a wide range of possible source body configurations and combinations can give rise to similar-looking anomalies. The effect that this ambiguity can have on modeling those anomalies can be reduced by designing filters to minimize or remove the unwanted components expected from known or plausible sources. In our area, a range of such sources can be expected in relation to its history of crustal thinning during continental breakup (Jokat et al., 2003).

In general, such margins are characterized by their continent-ocean transitions (COT). At their landward edges, the continental crust becomes thinner toward the adjacent ocean basins across a necking zone. Crustal densities tend not to vary greatly over necking zones, but the presence of denser mantle rocks at ever-shallower depths beneath gives rise to a general seaward increase in gravitational acceleration. Seaward of the necking zones, the crustal fabrics of COTs are highly variable and, in the absence of sampling by drilling, contentious. Some seem to have been strongly affected by magmatic processes, while others show evidence for extreme mechanical thinning of the crust that has left mantle rocks exposed at the seabed (e.g., Whitmarsh et al., 2001). Regardless of this complexity, however, seismic velocity records show that basement densities, and the attendant gravitational acceleration, increase seaward across all COTs until their depth functions are indistinguishable from those of basaltic igneous crust. Global surveys have shown the widths of extensional necking zones to be not less than 50–100 km (de Lépinay et al., 2016), and the mean width of COTs to be 170 km (Eagles et al., 2015). Two-dimensional gravity models constrained by bathymetric, seismic reflection, and refraction data show that the extended margin of the Riiser Larsen Sea and its conjugate in the Mozambique Basin fits these general patterns well and specifies that its COT is strongly affected by magmatism (Jokat et al., 2003, 2004; Leitchenkov et al., 2008; Leinweber et al., 2013; Müller & Jokat, 2019). Based on this, we expect the full wavelengths of gravity signals related to the crustal thinning not to be shorter than about 200 km, and that shorter-wavelength anomalies are likely to express some combination of magmatism-related density contrasts in the COT and seafloor topography.

Figure 4 depicts six cross-sections across our final 3-D topographic model in combination with observed, filtered, and calculated gravity anomalies, the model residuals, and magnetic anomalies. Panels (a) through (d) in Figure 4 are dip lines across the margin, showing how the long-wavelength gravity anomaly is strongly suppressed by the band-pass filter. Based on the considerations given above, we expect this filter to have removed the crustal thinning signal, and that the remaining anomalies in the 5–150 km band are therefore related to some combination of magmatism-related geological variability and bathymetry. Of these, the density model of Figure 3a shows that the expected geological/magmatic signal has been compensated for to some extent.

In more detail, the greater model densities close to the shelf edge (Figure 3a), and the onset of their increase along the southern edges of large magnetic anomalies as seen in Figure 4 (Ruppel et al., 2018; Mieth et al., 2014), are both consistent with the presence of doleritic and basaltic rocks typical of a magmatic COT. Similarly located magnetic anomalies in the conjugate Mozambique Basin and Explora margin of western Dronning Maud Land have both been attributed to the presence of continental breakup-related magmatic intrusions and wedge-shaped piles of seaward-dipping basalt flows (Hinz & Krause, 1982; Jokat et al., 2003, 2004; Kristoffersen et al., 2014; Leinweber et al., 2013; Müller & Jokat, 2017, 2019). Crustal gravity models in both of these settings do not require the seaward-dipping basalt wedges to present strong gravimetric signatures of their own (Jokat et al., 2004; Leinweber et al., 2013); their densities are too similar to those of the surrounding basement rocks. Expecting this to be the case in our study area, we note that the basalt-related magnetic anomaly does not coincide with any consistent pattern in our modeled bathymetry.

Panel (d) illustrates the effective modeling of bathymetric and geological signals particularly well. The availability of radar depth constraints from the Derwael Ice Rise makes it clear that the rise occurs at a culmination located near the shelf edge, and that the culmination is present and modelable over the band-pass-filtered and density-adjusted gravity high. Similarly, the coincidence of a bathymetric sill at the gravity high is undeniable at the pinning points PPhs and PPw, where Drews (2019b) and Mouginot et al. (2017a) infer the presence of grounded ice. In panels (a) through (c), the model features relatively large gravity residuals near the shelf edge. We attribute these residuals to the absence of a topographic correction for the steep seafloor slopes in those locations, although it is of course not possible to rule out a component of small-scale geological complexity in the COT. Panels (e) and (f) in Figure 4 run south of and parallel to the continental shelf and confirm the general fit of our filter choice to the available depth references.

2.6. Error Estimation

First-order estimations of water depths originating from gravity inversions are afflicted by unavoidable errors. In relation to the filter used to preprocess the gravity data, errors also arise from instrumental

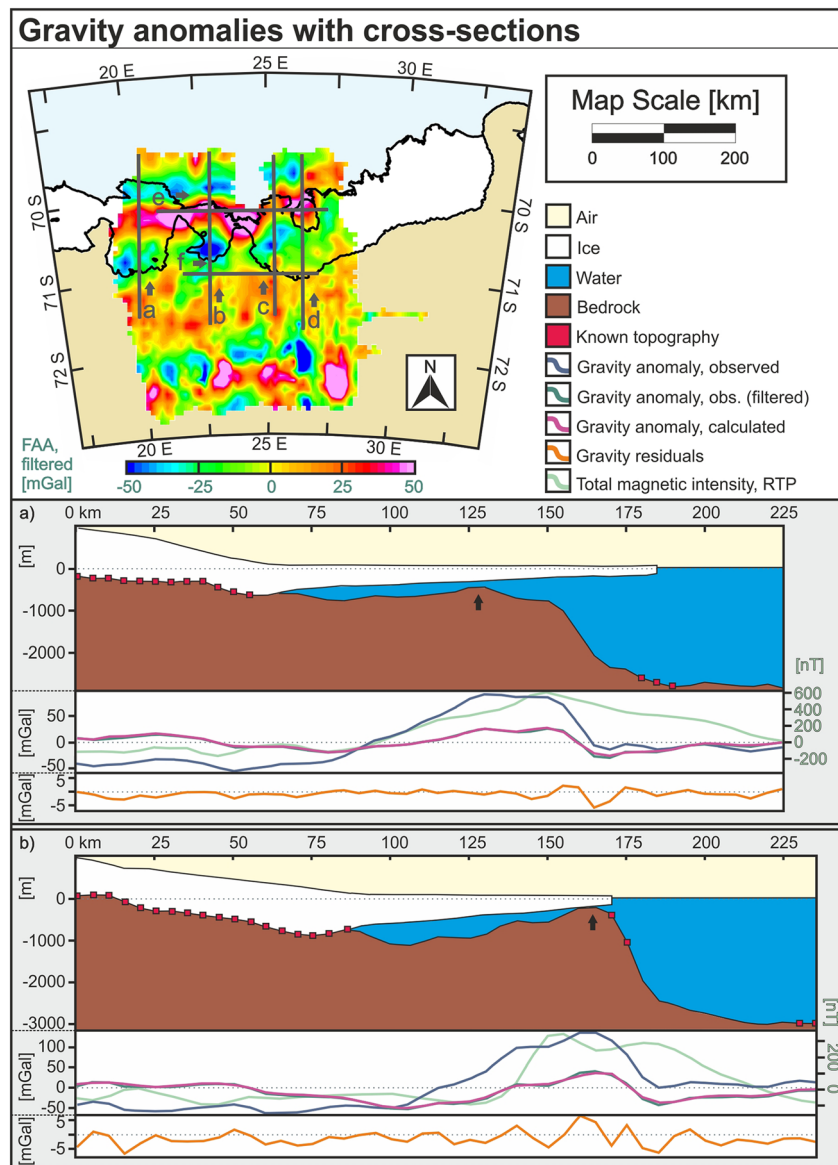


Figure 4. Fit of gravity anomalies to bedrock topography. Filtered free air gravity anomalies from Figure 2d with six cross-sections along flight lines incorporate observed and modeled bathymetry as well as the observed, filtered, and calculated gravity anomalies with resulting gravity residuals below. The total magnetic intensity (reduced to pole) is indicated in the background of gravity data (Mieth et al., 2014; Ruppel et al., 2018). Positions of bathymetric sills are indicated with black arrows. Depth panels (a) through (d) have a vertical exaggeration of 30, while panels (e) and (f) have a VE of 60. Grounding lines and ice shelf extents are extracted from Mouginot et al. (2017a).

inaccuracies during the data acquisition, the limitations of data processing, and as an inherent component of the modeling process.

Qualitatively, the greatest differences between reality and model are to be expected in the regions of steep seafloor slopes. Acquisition-related filtering and airspeed limitations constrain the spatial resolution of our gravity data to 6.3 km along track, and the unknown subglacial bathymetry precludes the application of a complete topographic correction. As a result, the bathymetry yielded by gravity inversion in regions of high bathymetric gradient will always overestimate the water depth at the head of a slope and underestimate it at the foot. The higher the bathymetric gradient, the more severe the differences between modeled and measured depths.

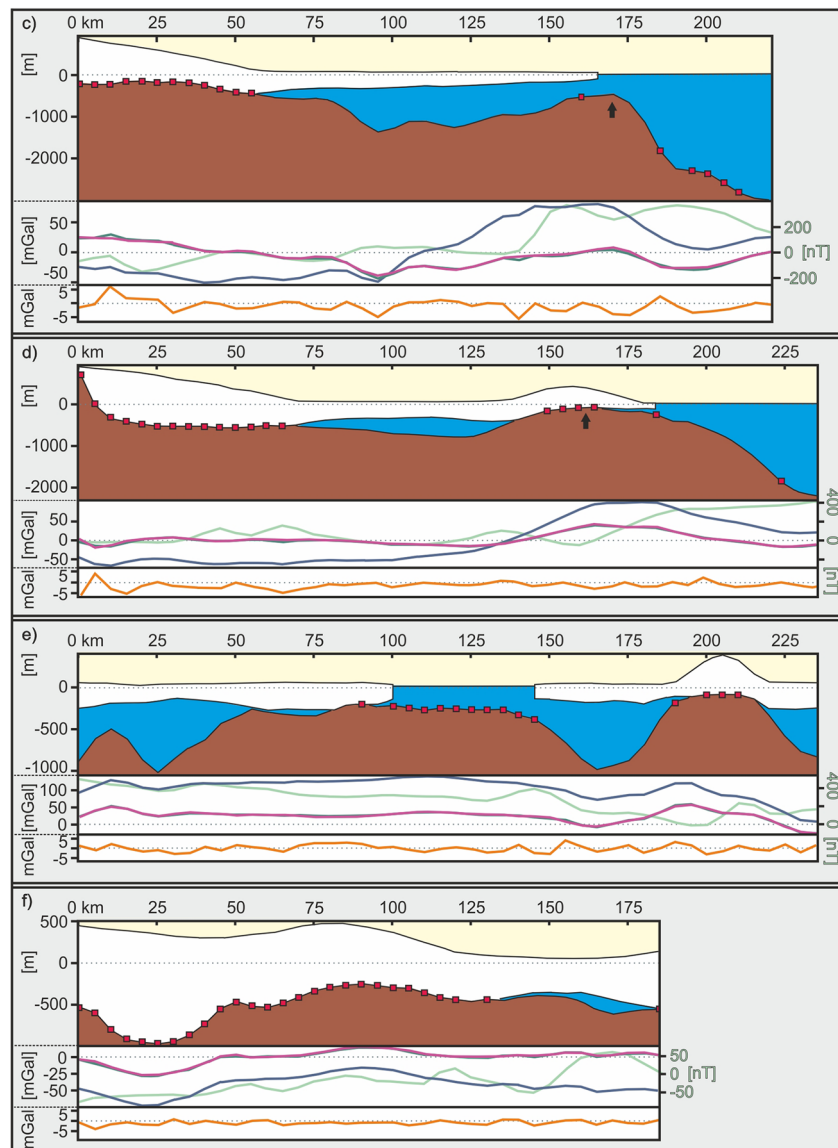


Figure 4. Continued.

Gravimeter instrumental inaccuracies experienced during acquisition are determined by postleveling cross-point analysis (standard deviation 5.8 mGal) rather than using the smaller theoretical accuracy. These cross-over errors build the basis for our error estimation.

Ice thickness errors of ± 20 m translate to the errors of approximately a tenth in the final bathymetric model underlying the ice shelves. The density contrast of the ice-water interface ($1,030-915 = 115 \text{ kg/m}^3$) is significantly lower than that of the water-seabed interface (with a starting bedrock density of $2,670 \text{ kg/m}^3$ [$2,670-1,030 = 1,640 \text{ kg/m}^3$]). However, the initial DC shift on the gravity data is mainly calculated using the ice/bedrock interface inferred from the radar data. Thus, the associated error in the ice-penetrating radar data affects the modeling process from the start and should be considered in its entirety in the overall error estimation.

Additionally, errors in our density model have to be accounted for. The density model allows for lateral deviations and is complemented across the unconstrained ice shelves by interpolation between better-constrained adjacent densities. These complemented densities vary by about $\pm 100 \text{ kg/m}^3$ from the mean bedrock density of 2670 kg/m^3 . Variation in this $\pm 100 \text{ kg/m}^3$ range is equivalent to about 8 mGal in gravity

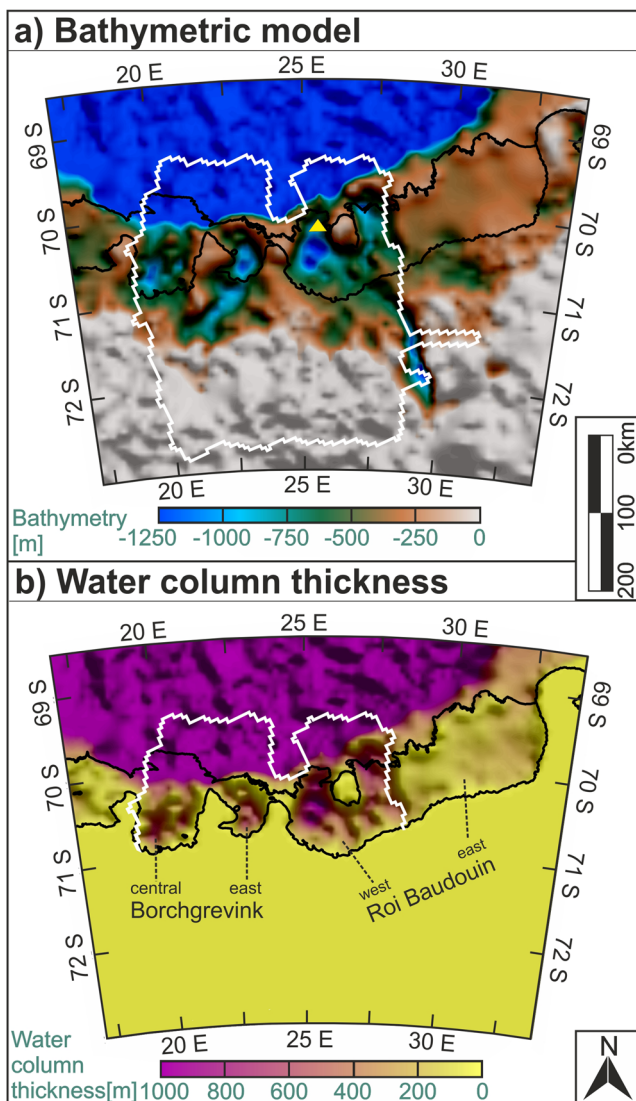


Figure 5. Bathymetric model. Bathymetric model (a) and water column thickness (b) across western RBIS and BIS. Bathymetry is referenced to the ellipsoid WGS84. White grid outlines show the extent of free air anomaly data used during gravity inversion. A supporting CTD cast from Favier et al. (2016) is shown as yellow triangle in panel (a). Outside the gravity grid, the seabed beneath the ice shelves and in the open ocean is implemented from Morlighem (2020b) and Arndt et al. (2013), respectively. Grounding lines and ice shelf extents are extracted from Mougnot et al. (2017a).

residuals over the constrained regions. We adopt this value as an estimate of the error related to geological uncertainty in the ice shelf regions.

The density contrast at the ocean-seabed interface is $1,640 \text{ kg/m}^3$, if using the mean bedrock density. Taking this contrast as the basis for a Bouguer slab calculation together with the crossover error of 5.8 mGal and the geologic variability of 8 mGal leads us to estimate that the modeled bathymetric uncertainties lie in the range $\pm 200 \text{ m}$. Combined with the uncertainty of ice-penetrating radar data, the total estimated uncertainty range of $\pm 220 \text{ m}$ is consistent with the previous empirically derived root mean square misfits between gravity-derived and seismic depths (Brisbourne et al., 2014; Greenbaum et al., 2015). An evenly distributed set of depth soundings across the ice shelves in our model area has the potential to decrease the overall error by a large margin. Additional data would improve the geological model significantly and minimize the error caused by an unknown geological variability.

Along-track resolution and line spacing impact on the accuracy and resolution of the modeled bathymetry. Cross-track interpolation may induce gridding artifacts that appear as bathymetric model errors. The along-track resolution strongly depends on acquisition parameters. Since the along-track resolution of gravity data is 6.3 km and the survey line spacings range between 5 and 10 km, the final bathymetric model is gridded with a resolution of 5 km.

3. Bathymetric Model Results

The bathymetric model generated within this study is limited to the GEA I-III gravity data grid extents (Figure 5a) and is presented relative to the WGS84 ellipsoid. Water column thicknesses (Figure 5b) are calculated using this model and the ice drafts extracted from the ice-penetrating radar data. The model shows deep troughs underlying thick water columns beneath the current main ice flows. These troughs cross the seafloor between the grounding lines and bathymetric sills close to the continental shelf. This pattern is similar to the one observed beneath ice shelves in the adjacent western part of DML, including the Ekström, Jelbart, and Fimbul ice shelves (Eisermann et al., 2020). Based on this and the considerations given in Section 2.5, we consider it highly unlikely that our model's bathymetric sills are the artifacts of poorly modeled magmatic variability at the Riiser Larsen margin. Further confidence in this view can be taken from the observation that pinning points PPw and the Derwael Ice Rise at the western RBIS (Figures 1c and 4, profile d), for example, both lie south of the magnetic anomaly that marks the presence of magmatic rocks near the shelf edge. In the following, the model is described in more detail, moving from west to east.

Modeled bathymetry beneath the central part of the BIS shows a depression of 1100 m in the south and a bathymetric sill running west–east close to the continental shelf break beneath the ice shelf's center (Figure 6, DD). The sill is interrupted by two gateways with their greatest depths at 620 m in the west and 600 m in the east. The shallowest point between the two mentioned gateways reaches a minimum water column thickness of just $\sim 30 \text{ m}$ over the sill (Figure 6, CC). The northern part of the central BIS segment overhangs the steep continental slope and rises by as much as 50 km (Figure 6, CC). The seafloor depth beneath the overhang ranges from hundreds of meters at the continental shelf break to the modeled and observed depths of more than 2000 m close to the calving front.

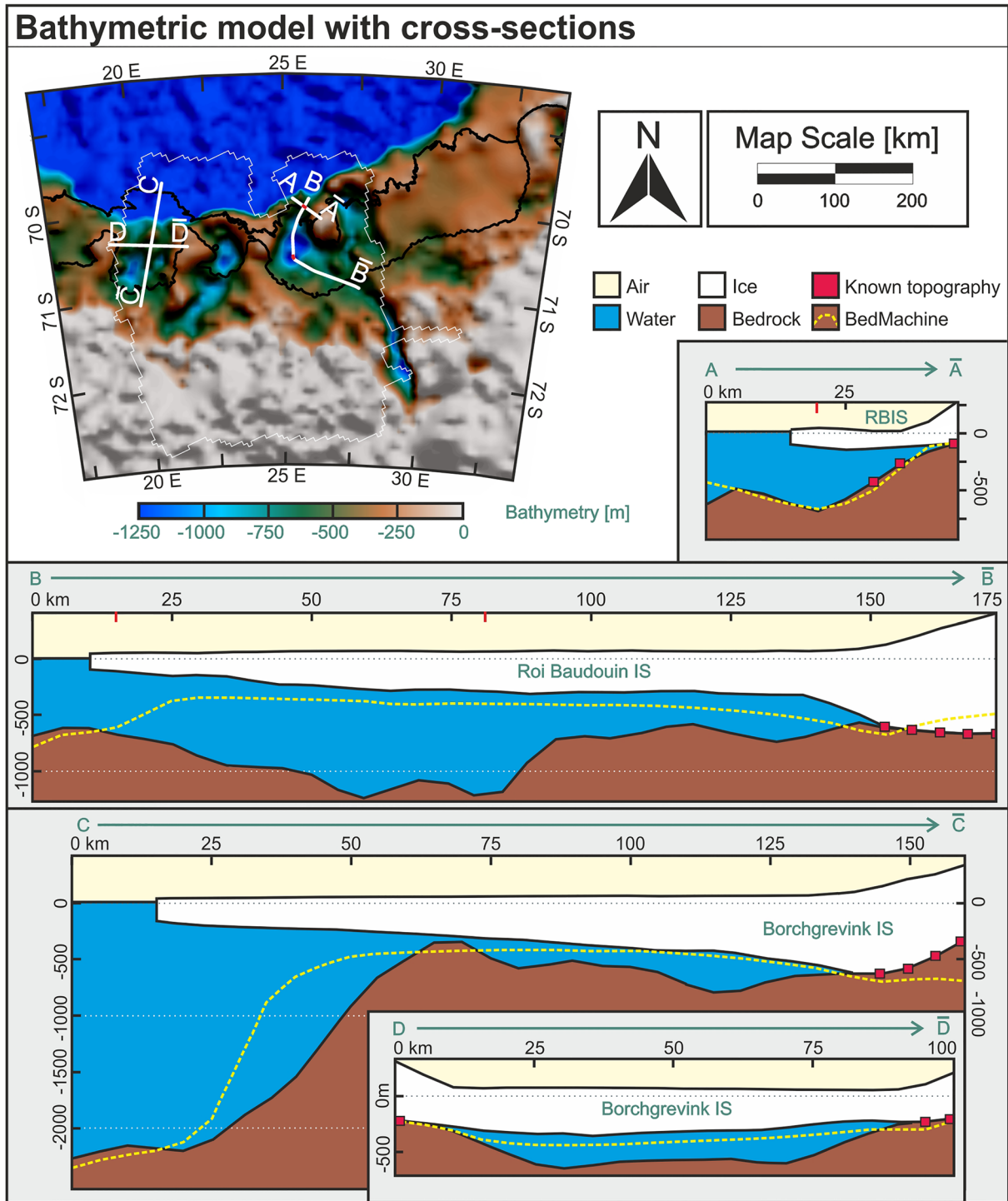


Figure 6. Bathymetric model with cross-sections. The overview depicts four 2D profiles (AA , BB , CC , and DD) showing cross-sections of the bathymetric model with its inherent resolution of 5 km. These 2-D sections share the same scale and vertical exaggeration of 20:1. Bedrock in the recent topographic compilation BedMachine Antarctica by Morlighem (2020) is marked with yellow dashed lines. Profiles AA and BB show the shallowest point of the gateway leading into the RBIS. This point and one other are marked red in the overview and 2D sections for orientation. BB also shows the course of the trough with a plateau close to the grounding line. Cross-section CC exhibits the central BIS overhanging the continental shelf by approximately 50 km and traverses a bathymetric high. The section DD displays the two distinct gateways neighboring this bathymetric high.

The bathymetry for both the eastern part of BIS and western RBIS show troughs that progress seaward from the grounding line, where they underlie moderate to thick ice shelf cavities. In the cavities, as Eisermann et al. (2020) observed for the ice shelves of western DML, the trough floors undulate rather than deepening monotonically seaward. The deepest points overall beneath the eastern BIS and western RBIS lie at 1180 m and 1320 m, respectively. The calving fronts of both ice shelf segments overlie bathymetric sills that perch on the continental shelf break. The sill beneath the eastern BIS is continuous and shallow, with average depths of 250 m. Its deepest point at 450 m in the west forms a shallow gateway. In contrast to the eastern BIS, however, the sill of the western RBIS is cut by a distinct deep gateway with a minimum depth of 630 m that lies along strike of the trough that steers toward the gap between PPw and the Derwael Ice Rise (Figure 6, \overline{AA} & \overline{BB}). To date, this is the deepest recorded or modeled gateway to any of DML's ice shelf cavities. The associated trough does not deepen smoothly to the deepest part of the southern grounding line, as proposed by Favier et al. (2016), but is instead interrupted by undulating topography (Figure 6, \overline{BB}).

The water column between the continental shelf and the BIS is relatively thin with sporadic exceptions. At its tallest points, the cavity reaches ~ 660 m in the central and ~ 630 m in the eastern part of the BIS. The water column between the continental slope and northern BIS is much taller and fully open to the ocean. Beneath the RBIS, maximum water column thicknesses of up to 1,000 m are modeled, west and east of the Derwael Ice Rise.

The available gravity data are too sparse to extend our model over the eastern RBIS. Based on our experience with other DML ice shelves, we expect that it is underlain by a seafloor of ~ 1 -km depth like that seen in the western RBIS. Figure 5a shows that the interpolated depths from Morlighem et al.'s (2020) compilation and mass-conservation model are much shallower than this expectation in the range of 200–400 m. These depths are comparable to prevalent ice base depths resulting in strongly underestimated water column thicknesses in Figure 5b. Similarly, replacing interpolated depths with modeled depths in our research area sees a $\sim 100\%$ increase in cavity volume beneath the BIS and western RBIS from $\sim 6,000$ km³ (Morlighem, 2020) to $\sim 12,000$ km³. Considering that both the BIS and RBIS are sites of significant ongoing ice mass loss (Rignot et al., 2013), this underlines the necessity for the updated bathymetric models even of small ice shelves.

4. Discussion

4.1. Ice Shelf Stability

Currently, both RBIS and BIS are regarded as cold-cavity ice shelves and are considered to be in equilibrium (Rignot et al., 2013). This is to say that water masses circulating in the cavities are thought to be largely below melting temperatures. Despite this, the steep continental slope and narrow continental shelf in DML, and specifically the Riiser-Larsen Sea (Figure 1c), represent preconditions for strong variability in water mass and heat exchange between the open ocean and cavities. One such variation is the possible intrusion of WDW into the cavities, which could lead to increased basal melt rates. With updated bathymetry at hand, the WDW ingress into the cavities can be estimated. In doing so, the estimated error envelope of ± 220 m should always be considered. Full utilization of the error can drastically change interpretation, especially in crucial areas, such as along the shelf-edge sills. The bathymetric model is, however, a vast improvement over the recent topographic compilations (Fretwell et al., 2013; Morlighem et al., 2020) that are solely based on interpolation between points of constraints. An increase of 100% in cavity volume within our model area, compared to the topographic data set by Morlighem (2020) underlines this improvement.

Warm water inflow has already been observed off the mouth of the trough that crosses the western RBIS, using a CTD cast to a maximum depth of about 850 m (Figure 5; Berger, 2017; Callens, 2014; Favier et al., 2016). The shallowest point along this trough is at the 630 (± 220)-m-deep gateway along the bathymetric sill at the continental shelf break (Figures 5 and 6, \overline{AA}), coinciding with a rise in water temperature between 600 and 650 m that represents WDW (CTD cast in Figure 5; Berger, 2017; Callens, 2014). Also, this point lies deeper than the average thermocline of 600 m in water depths of 1,000 m, as observed for example at the Fimbul Ice Shelf 700 km further west (Hattermann, 2018). WDW that breaches the sill and enters the RBIS' cavity could thus be efficiently transported to the grounding line through the trough. This might explain the high basal melt rates beneath the ice shelf (Rignot et al., 2013; Berger et al., 2017; Sun et al., 2019).

A similar interpretation is possible for the central BIS. With gateways at about 600 (± 220)-m depth, WDW is likely to intrude into the cavity, at least sporadically. In addition to this, the ice shelf overhangs the sill and continental shelf break by ~ 50 km and is heavily exposed to the open ocean with water depths of more than 2,000 m (Figure 6, CC), causing its exposure to warmer water temperatures due to thermocline shallowing (Hattermann et al., 2014). This vulnerability is reflected in its dominant mass loss process, iceberg calving (Rignot et al., 2013). Whether the overhang is an equilibrium feature of the BIS is open to question. It may be a reflection of an ongoing post-1994 increase in ice flow velocities (Gudmundsson et al., 2019), which may be the consequence of a foregoing unpinning of the ice shelf near its center. Certainly, bathymetry beneath the central BIS is generally shallow with a central high at 310 m that may until recently have acted as a pinning point (Figure 6, CC), similar to the situation at the Jelbart Ice Shelf further west (Eisermann et al., 2020). The bathymetric sill of the eastern BIS is shallower and lacks deep gateways to the cavities over the continental shelf.

Marine-outlet glaciers with retrograde to flat beds may retreat over the coming century as warming ocean waters interact with their bases, forcing their grounding lines to move upstream (Gudmundsson et al., 2012; Hellmer et al., 2012). In eastern DML, Favier et al. (2016) prognosed this so-called marine ice sheet instability specifically for the Hansenbreen. Callens et al. (2014) observed a similar setting at the WRG leading into the RBIS. Recent modeling has suggested, in contrast, that the RBIS has been in a relatively stable condition over recent millennia (Berger et al., 2016; Favier & Pattyn, 2015). Our identification of a larger cavity with an open ocean connection via a deep gateway leads to the question of whether that modeling may have underestimated the possibility for the past (and future) periods of sustained warm water inflow and related retreat of the RBIS-WRG system.

4.2. Glacial History

The landscape of DML has been shaped by tectonic processes as well as fluvial and glacial erosion. Inland of the region's coastal escarpments, the observation of subglacially preserved alpine landscapes connected with an intact and only slightly modified fluvial drainage system speaks for a period of alpine style glaciation before the formation of cold-based ice sheets (Eagles et al., 2018; Franke et al., 2021; Näslund, 2001). Seaward, the subglacial topography and bathymetry in DML suggests a different history, being characterized overall by gentle slopes crossed by overdeepened troughs with undulating valley profiles that terminate at prominent sills along the continental shelf break (Eisermann et al., 2020; Nøst, 2004; Smith et al., 2020). These patterns testify to the erosive and depositional power of a mobile grounded ice sheet.

Hence, as for the ice shelves of western DML, we propose that the sills near the present-day calving fronts of the BIS and RBIS comprise end moraines deposited at the grounding line during the Last Glacial Maximum at 23–19 k yrs BP (Grobe & Mackensen, 1992; Mackintosh et al., 2014). Phases of glacial advance also saw erosion of the trough floors that resulted in overdeepened basins along their lengths, much like those observed in the bathymetric models of the Fimbul, Jelbart, and Ekström ice shelves in western DML (Eisermann et al., 2020). The implication is of synchronous phases of grounding line retreat and advance throughout DML.

The modeled overdeepened basins likely prevented regrounding of ice shelves in eastern DML except at pinning points and the ice rises close to the calving front. However, the central BIS has a different setting with quite shallow bathymetry directly beneath its center, comparable to the Jelbart Ice Shelf (Eisermann et al., 2020). Partitioning of the central BIS cavity into two sections separated by a central bathymetric high can be explained by its excavation at some time in the past by the same two main ice streams (Figure 1c) that currently feed the ice shelf.

5. Summary

Bathymetry beneath the central and eastern parts of the BIS and for the western RBIS was modeled by the inversion of gravity data. Comparison of this model to interpolations in a recent topographic compilation (Morlighem et al., 2020) has shown that the volumes of cavities beneath these ice shelves have been underestimated by $\sim 100\%$. The picture of consistently deeper bathymetry significantly reduces the likelihood that

past or future retreat episodes of DML's ice shelves would have been, or might be, interrupted by regrounding events at pinning points.

The shape of the seabed and the height of the water column beneath these two ice shelves show many similarities with the models of ice shelves in western DML (Eisermann et al., 2020). The bathymetry beneath DML's ice shelves has deep bathymetric troughs traversing the continental shelves and terminating behind bathymetric saddles on otherwise continuous sills along the continental shelf break. In detail, the trough floor profiles undulate through the overdeepenings and moraines that record details of the region's recent glacial history.

The differing dominant mass loss processes of the RBIS and BIS are reflected in their settings. While mass loss from the BIS is dominated by iceberg calving, mass loss from the RBIS is dominated by basal melting (Rignot et al., 2013). The high rate of iceberg calving at BIS could be induced by the exposure of its northern part to the open ocean in combination with a recent unpinning of the ice shelf. The RBIS on the other hand is probably mainly exposed to WDW ingress, due to its single deep gateway combined with the otherwise high rate of isolation due to the bathymetric sill, leading to a dominance of basal melt.

The gateways along the bathymetric sills represent known (in western DML, Eisermann et al., 2020) or likely points of ingress for WDW into the ice shelf cavities. The most significant gateways in this study occur near the snout of the main trough traversing the western RBIS and beneath the central BIS. These points mark relatively deep gateways in respect to other ice shelves of DML (Eisermann et al., 2020) and should be regarded as threats to future ice shelf stability.

Data Availability Statement

The bathymetric model generated in this study, together with observed, filtered, and calculated gravity data with resulting gravity residuals, is available on Pangaea (<https://doi.org/10.1594/PANGAEA.927545>). Additional topographic data sources used in this study are listed in the references.

Acknowledgments

The GEA program is jointly funded by the Alfred Wegener Institute, Helmholtz Centre for Polar and Marine Research, and the Federal Institute for Geosciences and Natural Resources (BGR). The airborne campaigns would not have been possible without the crews from Kenn Borek Air Ltd and the technical and logistical support of the Princess Elisabeth station. We are thankful to GEA science leaders Matthias Mieth and Daniel Steinhage as well as for the technical and logistical expertise of Alfred Wegener Institute technicians for ensuring the successful implementations of three airborne campaigns. Antonia Ruppel and Andreas Läufer acknowledge funding by the Deutsche Forschungsgemeinschaft (DFG) within the frame of the Collaborative Research Programme SPP 1158 "Antarctic Research with comparative investigations in Arctic ice areas" (grants LA1080/9 to Andreas Läufer and LI 745/15 to Frank Lisker). The authors would like to thank Emerson E&P Software, Emerson Automation Solutions, for providing licenses for the seismic software Paradigm in the scope of the Emerson Academic Program. We are highly grateful to reviews by Atsuhiko Muto and two anonymous reviewers that greatly enhanced the manuscript. Open access funding enabled and organized by Projekt DEAL.

References

- Arndt, J. E., Schenke, H. W., Jakobsson, M., Nitsche, F. O., Buys, G., Goleby, B., et al. (2013). The International Bathymetric Chart of the Southern Ocean (IBCSO) Version 1.0—A new bathymetric compilation covering circum-Antarctic waters. *Geophysical Research Letters*, 40(12), 3111–3117. <https://doi.org/10.1002/grl.50413>
- Berger, S. (2017). *Stability of Antarctic ice shelves: A case study of the Roi Baudouin Ice Shelf, Dronning Maud Land, East Antarctica (Doctoral dissertation)*. Université Libre de Bruxelles.
- Berger, S., Drews, R., Helm, V., Sun, S., & Pattyn, F. (2017). Detecting high spatial variability of ice shelf basal mass balance, Roi Baudouin Ice Shelf, Antarctica. *The Cryosphere*, 11(6), 2675–2690. <https://doi.org/10.5194/tc-11-2675-2017>
- Berger, S., Favier, L., Drews, R., Derwael, J. J., & Pattyn, F. (2016). The control of an uncharted pinning point on the flow of an Antarctic ice shelf. *Journal of Glaciology*, 62(231), 37–45. <https://doi.org/10.1017/jog.2016.7>
- Blindow, N. (1994). The central part of the Filchner-Ronne Ice Shelf, Antarctica: Internal structures revealed by 40MHz monopulse RES. *Annals of Glaciology*, 20, 365–371. <https://doi.org/10.3189/1994aog20-1-365-371>
- Brisbourne, A., Smith, A., King, E., Nicholls, K., Holland, P., & Makinson, K. (2014). Seabed topography beneath Larsen C Ice Shelf from seismic soundings. *The Cryosphere*, 8(1), 1–13. <https://doi.org/10.5194/tc-8-1-2014>
- Callens, D. (2014). *Impact of improved basal and surface boundary conditions on the mass balance of the Sr Rondane Mountains glacial system, Dronning Maud Land, Antarctica (Doctoral dissertation)*. Université libre de Bruxelles.
- Callens, D., Matsuoka, K., Steinhage, D., & Pattyn, F. (2015). Surface elevation and ice thickness measurements of an airborne radar survey made in the Sor Rondane Mountains, Antarctica. *PANGAEA*. <https://doi.org/10.1594/PANGAEA.836299>
- Callens, D., Matsuoka, K., Steinhage, D., Smith, B., Wittrant, E., & Pattyn, F. (2014). Transition of flow regime along a marine-terminating outlet glacier in East Antarctica. *The Cryosphere*, 8(3), 867–875. <https://doi.org/10.5194/tc-8-867-2014>
- Carmack, E. C., & Foster, T. D. (1975). *On the flow of water out of the Weddell Sea Deep sea research and oceanographic Abstracts*. Paper presented at the.
- de Lépinay, M. M., Loncke, L., Basile, C., Roest, W. R., Patriat, M., Maillard, A., & De Clarens, P. (2016). Transform continental margins—Part 2: A worldwide review. *Tectonophysics*, 693, 96–115. <https://doi.org/10.1016/j.tecto.2016.05.038>
- Depoorter, M. A., Bamber, J. L., Griggs, J. A., Lenaerts, J. T., Ligtenberg, S. R., van den Broeke, M. R., & Moholdt, G. (2013). Calving fluxes and basal melt rates of Antarctic ice shelves. *Nature*, 502(7469), 89–92. <https://doi.org/10.1038/nature12567>
- Derwael, J. (1985). *Levés Altimétriques - BRB - Côte Princesse Ragnild, Expéditions Antarctiques Belgo-Néerlandaises (5 maps)*. Exantar.
- Drews, R. (2019a). Ice thickness, surface-, and bed elevation of Derwael Ice Rise, Dronning Maud Land Antarctica (2012–2013). *PANGAEA*. <https://doi.org/10.1594/PANGAEA.905315>
- Drews, R. (2019b). Ice thickness, surface-, and bed elevation of a pinning point in Roi Baudouin Ice Shelf, Dronning Maud Land Antarctica. *PANGAEA*. <https://doi.org/10.1594/PANGAEA.905997>
- Drews, R., Matsuoka, K., Martin, C., Callens, D., Bergeot, N., & Pattyn, F. (2015). Evolution of Derwael Ice Rise in Dronning Maud Land, Antarctica, over the last millennia. *Journal of Geophysical Research: Earth Surface*, 120(3), 564–579. <https://doi.org/10.1002/2014jf003246>

- Drews, R., Pattyn, F., Hewitt, I. J., Ng, F. S. L., Berger, S., Matsuoka, K., et al. (2017). Actively evolving subglacial conduits and eskers initiate ice shelf channels at an Antarctic grounding line. *Nature Communications*, 8(1), 1–10. <https://doi.org/10.1038/ncomms15228>
- Dupont, T., & Alley, R. B. (2005). Assessment of the importance of ice-shelf buttressing to ice-sheet flow. *Geophysical Research Letters*, 32(4). <https://doi.org/10.1029/2004GL022024>
- Eagles, G., Karlsson, N. B., Ruppel, A., Steinhage, D., Jokat, W., & Läufer, A. (2018). Erosion at extended continental margins: Insights from new aerogeophysical data in eastern Dronning Maud Land. *Gondwana Research*, 63, 105–116. <https://doi.org/10.1016/j.gr.2018.05.011>
- Eagles, G., Pérez-Díaz, L., & Scarselli, N. (2015). Getting over continent ocean boundaries. *Earth-Science Reviews*, 151, 244–265. <https://doi.org/10.1016/j.earscirev.2015.10.009>
- Eisermann, H., Eagles, G., Ruppel, A., Läufer, A., & Jokat, W. (2021). Modeled bathymetry beneath Roi Baudouin and Borchgrevink ice shelves, east Antarctica. *PANGAEA*. <https://doi.pangaea.de/10.1594/PANGAEA.927545>
- Eisermann, H., Eagles, G., Ruppel, A., Smith, E. C., & Jokat, W. (2020). Bathymetry beneath ice shelves of Western Dronning Maud Land, East Antarctica, and implications on ice shelf stability. *Geophysical Research Letters*, 47(12), e2019GL086724. <https://doi.org/10.1029/2019gl086724>
- Elburg, M. A., Andersen, T., Jacobs, J., Läufer, A., Ruppel, A., Krohne, N., & Damaske, D. (2016). One hundred fifty million years of intrusive activity in the Sør Rondane Mountains (East Antarctica): Implications for Gondwana assembly. *The Journal of Geology*, 124(1), 1–26. <https://doi.org/10.1086/684052>
- Favier, L., Gagliardini, O., Durand, G., & Zwinger, T. (2012). A three-dimensional full Stokes model of the grounding line dynamics: Effect of a pinning point beneath the ice shelf. *The Cryosphere*, 6(1), 101–112. <https://doi.org/10.5194/tc-6-101-2012>
- Favier, L., & Pattyn, F. (2015). Antarctic ice rise formation, evolution, and stability. *Geophysical Research Letters*, 42(11), 4456–4463. <https://doi.org/10.1002/2015gl064195>
- Favier, L., Pattyn, F., Berger, S., & Drews, R. (2016). Dynamic influence of pinning points on marine ice-sheet stability: A numerical study in Dronning Maud Land, East Antarctica. *The Cryosphere*, 10(6), 2623–2635. <https://doi.org/10.5194/tc-10-2623-2016>
- Franke, S., Eisermann, H., Jokat, W., Eagles, G., Asseng, J., Miller, H., et al. (2021). Preserved landscapes underneath the Antarctic Ice Sheet reveal the geomorphological history of Jutulstraumen Basin. *Earth Surface Processes and Landforms*. <https://doi.org/10.1002/esp.5203>
- Fretwell, P., Pritchard, H. D., Vaughan, D. G., Bamber, J. L., Barrand, N. E., Bell, R., et al. (2013). Bedmap2: Improved ice bed, surface and thickness datasets for Antarctica. *The Cryosphere*, 7(1), 375–393. <https://doi.org/10.5194/tc-7-375-2013>
- Goldberg, D., Gourmelen, N., Kimura, S., Millan, R., & Snow, K. (2019). How accurately should we model ice shelf melt rates? *Geophysical Research Letters*, 46(1), 189–199. <https://doi.org/10.1029/2018GL080383>
- Golynsky, A. V., Masolov, V. N., Nogi, Y., Shibuya, K., Tarlowy, C., & Wellman, P. (1996). Magnetic anomalies of Precambrian terranes of the East Antarctic shield coastal region (20° E–50° E). *Paper presented at the Proceedings of the NIPR Symposium on Antarctic Geosciences*.
- Grantham, G., Maboko, M., & Eglinton, B. (2003). A review of the evolution of the Mozambique Belt and implications for the amalgamation and dispersal of Rodinia and Gondwana. *Geological Society, London, Special Publications*, 206(1), 401–425. <https://doi.org/10.1144/GSL.SP.2003.206.01.19>
- Greenbaum, J. S., Blankenship, D. D., Young, D. A., Richter, T. G., Roberts, J. L., Aitken, A. R. A., et al. (2015). Ocean access to a cavity beneath Totten Glacier in East Antarctica. *Nature Geoscience*, 8(4), 294–298. <https://doi.org/10.1038/Ngeo2388>
- Grobe, H., & Mackensen, A. (1992). Late quaternary climatic cycles as recorded in sediments from the Antarctic continental margin. The Antarctic paleoenvironment: A perspective on global change. *Antarctic Research Series*, 56, 349–376.
- Gudmundsson, G. H., Krug, J., Durand, G., Favier, L., & Gagliardini, O. (2012). The stability of grounding lines on retrograde slopes. *The Cryosphere*, 6(6), 1497–1505. <https://doi.org/10.5194/tc-6-1497-2012>
- Gudmundsson, G. H., Paolo, F. S., Adusumilli, S., & Fricker, H. A. (2019). Instantaneous Antarctic ice-sheet mass loss driven by thinning ice shelves. *Geophysical Research Letters*, 46(13), 903909–913909. <https://doi.org/10.1029/2019GL085027>
- Haseloff, M., & Sergienko, O. V. (2018). The effect of buttressing on grounding line dynamics. *Journal of Glaciology*, 64(245), 417–431. <https://doi.org/10.1017/jog.2018.30>
- Hattermann, T. (2018). Antarctic thermocline dynamics along a narrow shelf with easterly winds. *Journal of Physical Oceanography*, 48(10), 2419–2443. <https://doi.org/10.1175/Jpo-D-18-0064.1>
- Hattermann, T., Smedsrud, L. H., Nost, O. A., Lilly, J. M., & Galton-Fenzi, B. K. (2014). Eddy-resolving simulations of the Fimbul Ice Shelf cavity circulation: Basal melting and exchange with open ocean. *Ocean Modelling*, 82, 28–44. <https://doi.org/10.1016/j.ocemod.2014.07.004>
- Hellmer, H. H., Kauker, F., Timmermann, R., Determann, J., & Rae, J. (2012). Twenty-first-century warming of a large Antarctic ice-shelf cavity by a redirected coastal current. *Nature*, 485(7397), 225–228. <https://doi.org/10.1038/nature11064>
- Hinz, K., & Krause, W. (1982). The continental margin of Queen Maud Land, Antarctica: Seismic sequences, structural elements and geological development. *Geologisches Jahrbuch*, 23, 17–41.
- Howat, I. M., Porter, C., Smith, B. E., Noh, M. J., & Morin, P. (2019). The reference elevation model of Antarctica. *The Cryosphere*, 13(2), 665–674. <https://doi.org/10.5194/tc-13-665-2019>
- Jacobs, J., Elburg, M., Läufer, A., Kleinhanns, I. C., Henjes-Kunst, F., Estrada, S., et al. (2015). Two distinct late Mesoproterozoic/early Neoproterozoic basement provinces in central/eastern Dronning Maud Land, East Antarctica: The missing link, 15–21 E. *Precambrian Research*, 265, 249–272. <https://doi.org/10.1016/j.precamres.2015.05.003>
- Jacobs, J., & Thomas, R. J. (2004). Himalayan-type indenter-escape tectonics model for the southern part of the late Neoproterozoic-early Paleozoic East African-Antarctic orogen. *Geology*, 32(8), 721–724. <https://doi.org/10.1130/G20516.1>
- Jokat, W., Boebel, T., Koenig, M., & Meyer, U. (2003). Timing and geometry of early Gondwana breakup. *Journal of Geophysical Research*, 108(B9), 2428. <https://doi.org/10.1029/2002JB001802>
- Jokat, W., Ritzmann, O., Reichert, C., & Hinz, K. (2004). Deep crustal structure of the continental margin off the Explora Escarpment and the Lazarew Sea, East Antarctica. *Marine Geophysical Researches*, 25(3/4), 283–304. <https://doi.org/10.1007/s11001-005-1337-9>
- Kristoffersen, Y., Hofstede, C., Diez, A., Blenkner, R., Lambrecht, A., Mayer, C., & Eisen, O. (2014). Reassembling Gondwana: A new high quality constraint from vibroseis exploration of the sub-ice shelf geology of the East Antarctic continental margin. *Journal of Geophysical Research: Solid Earth*, 119(12), 9171–9182. <https://doi.org/10.1002/2014JB011479>
- Leinweber, V. T., Klingelhoefer, F., Neben, S., Reichert, C., Aslanian, D., Matias, L., et al. (2013). The crustal structure of the Central Mozambique continental margin—Wide-angle seismic, gravity and magnetic study in the Mozambique Channel, Eastern Africa. *Tectonophysics*, 599, 170–196. <https://doi.org/10.1016/j.tecto.2013.04.015>

- Leitchenkov, G., Guseva, J., Gandyukhin, V., Grikurov, G., Kristoffersen, Y., Sand, M., et al. (2008). Crustal structure and tectonic provinces of the Riiser-Larsen Sea area (East Antarctica): Results of geophysical studies. *Marine Geophysical Research*, 29(2), 135–158. <https://doi.org/10.1007/s11001-008-9051-z>
- Mackintosh, A. N., Verleyen, E., O'Brien, P. E., White, D. A., Jones, R. S., McKay, R., et al. (2014). Retreat history of the East Antarctic ice sheet since the last glacial maximum. *Quaternary Science Reviews*, 100, 10–30. <https://doi.org/10.1016/j.quascirev.2013.07.024>
- Meert, J. G. (2003). A synopsis of events related to the assembly of eastern Gondwana. *Tectonophysics*, 362(1–4), 1–40. [https://doi.org/10.1016/S0040-1951\(02\)00629-7](https://doi.org/10.1016/S0040-1951(02)00629-7)
- Meert, J. G., Vandervoo, R., & Ayub, S. (1995). Paleomagnetic investigation of the Neoproterozoic Gagwe Lavas and Mbozi Complex, Tanzania and the Assembly of Gondwana. *Precambrian Research*, 74(4), 225–244. [https://doi.org/10.1016/0301-9268\(95\)00012-T](https://doi.org/10.1016/0301-9268(95)00012-T)
- Mieth, M., Jacobs, J., Ruppel, A., Damaske, D., Laufer, A., & Jokat, W. (2014). New detailed aeromagnetic and geological data of eastern Dronning Maud Land: Implications for refining the tectonic and structural framework of Sor Rondane, East Antarctica. *Precambrian Research*, 245, 174–185. <https://doi.org/10.1016/j.precamres.2014.02.009>
- Morlighem, M. (2020). *MEaSURES BedMachine Antarctica, Version 2*. Boulder, CO: NASA National Snow and Ice Data Center Distributed Active Archive Center. <https://doi.org/10.5067/E1QL9HFQ7A8M>
- Morlighem, M., Rignot, E., Binder, T., Blankenship, D., Drews, R., Eagles, G., et al. (2020). Deep glacial troughs and stabilizing ridges unveiled beneath the margins of the Antarctic ice sheet. *Nature Geoscience*, 13(2), 132–137. <https://doi.org/10.1038/s41561-019-0510-8>
- Mouginot, J., Scheuchl, B., & Rignot, E. (2017a). *MEaSURES Antarctic Boundaries for IPY 2007-2009 from Satellite Radar, Version 2*. Boulder, CO: NASA National Snow and Ice Data Center Distributed Active Archive Center. <https://doi.org/10.5067/AXE4121732AD>
- Mouginot, J., Scheuchl, B., & Rignot, E. (2017b). *MEaSURES Annual Antarctic ice velocity maps 2005-2017, Version 1. [2016-2017]*. Boulder, CO: NASA National Snow and Ice Data Center Distributed Active Archive Center. <https://doi.org/10.5067/9T4EPQXTJYW9>
- Müller, C. O., & Jokat, W. (2017). Geophysical evidence for the crustal variation and distribution of magmatism along the central coast of Mozambique. *Tectonophysics*, 712, 684–703. <https://doi.org/10.1016/j.tecto.2017.06.007>
- Müller, C. O., & Jokat, W. (2019). The initial Gondwana break-up: A synthesis based on new potential field data of the Africa-Antarctica Corridor. *Tectonophysics*, 750, 301–328. <https://doi.org/10.1016/j.tecto.2018.11.008>
- Näslund, J. (2001). Landscape development in western and central Dronning Maud Land, East Antarctica. *Antarctic Science*, 13(3), 302–311. <https://doi.org/10.1017/S0954102001000438>
- Nicholls, K. W., Østerhus, S., Makinson, K., Gammelsrød, T., & Fahrbach, E. (2009). Ice-ocean processes over the continental shelf of the southern Weddell Sea, Antarctica: A review. *Reviews of Geophysics*, 47(3). <https://doi.org/10.1029/2007RG000250>
- Nishio, F., Ishikawa, M., Ohmae, H., Takahashi, S., & Katsushima, T. (1984). A preliminary study of glacial geomorphology in area between Breid Bay and the Sør Rondane mountains in Queen Maud Land, East Antarctica.
- Nixdorf, U., Steinhage, D., Meyer, U., Hempel, L., Jenett, M., Wachs, P., & Miller, H. (1999). The newly developed airborne radio-echo sounding system of the AWI as a glaciological tool. *Annals of Glaciology*, 29, 231–238. <https://doi.org/10.3189/172756499781821346>
- Nøst, O. A. (2004). Measurements of ice thickness and seabed topography under the Fimbul Ice Shelf, Dronning Maud Land, Antarctica. *Journal of Geophysical Research*, 109(C10). <https://doi.org/10.1029/2004JC002277>
- Parker, R. (1973). The rapid calculation of potential anomalies. *Geophysical Journal International*, 31(4), 447–455. <https://doi.org/10.1111/j.1365-246X.1973.tb06513.x>
- Riedel, S., Jokat, W., & Steinhage, D. (2012). Mapping tectonic provinces with airborne gravity and radar data in Dronning Maud Land, East Antarctica. *Geophysical Journal International*, 189(1), 414–427. <https://doi.org/10.1111/j.1365-246X.2012.05363.x>
- Rignot, E., Jacobs, S., Mouginot, J., & Scheuchl, B. (2013). Ice-shelf melting around Antarctica. *Science*, 341(6143), 266–270. <https://doi.org/10.1126/science.1235798>
- Ruppel, A., Jacobs, J., Eagles, G., Läufer, A., & Jokat, W. (2018). New geophysical data from a key region in East Antarctica: Estimates for the spatial extent of the Tonian Oceanic Arc Super Terrane (TOAST). *Gondwana Research*, 59, 97–107. <https://doi.org/10.1016/j.gr.2018.02.019>
- Ruppel, A. S., Jacobs, J., Läufer, A., Ratschbacher, L., Pfänder, J. A., Sonntag, B.-L., et al. (2020). Protracted late Neoproterozoic–early Palaeozoic deformation and cooling history of Sor Rondane, East Antarctica, from 40Ar/39Ar and U–Pb geochronology. *Geological Magazine*, 158, 1–655. <https://doi.org/10.1017/S0016756820000746>
- Schenke, H. W., Gütz, S., Iffland, A., & Obermüller, A. (2010). Swath sonar bathymetry during POLARSTERN cruise ANT-XX/2 (PS63) with links to multibeam raw data files. <https://doi.org/10.1594/PANGAEA.733040>
- Smith, E. C., Hattermann, T., Kuhn, G., Gaedicke, C., Berger, S., Drews, R., et al. (2020). Detailed seismic bathymetry beneath Ekström Ice Shelf, Antarctica: Implications for glacial history and ice-ocean interaction. *Geophysical Research Letters*, 47, e2019GL086187. <https://doi.org/10.1029/2019GL086187>
- Sun, S., Hattermann, T., Pattyn, F., Nicholls, K. W., Drews, R., & Berger, S. (2019). Topographic shelf waves control seasonal melting near Antarctic ice shelf grounding lines. *Geophysical Research Letters*, 46(16), 9824–9832. <https://doi.org/10.1029/2019gl083881>
- Tinto, K. J., Bell, R. E., Cochran, J. R., & Münchow, A. (2015). Bathymetry in Petermann fjord from operation IceBridge aerogravity. *Earth and Planetary Science Letters*, 422, 58–66. <https://doi.org/10.1016/j.epsl.2015.04.009>
- Voß, W., Daschner, S., & Schenke, H. W. (2011). Swath sonar bathymetry during POLARSTERN cruise ANT-XVII/2 (PS56) with links to multibeam raw data files. <https://doi.org/10.1594/PANGAEA.763731>
- Watts, A. B., & Moore, J. D. P. (2017). Flexural isostasy: Constraints from gravity and topography power spectra. *Journal of Geophysical Research: Solid Earth*, 122, 8417–8430. <https://doi.org/10.1002/2017jb014571>
- Whitmarsh, R. B., Manatschal, G., & Minshull, T. A. (2001). Evolution of magma-poor continental margins from rifting to seafloor spreading. *Nature*, 413, 150–154. <https://doi.org/10.1029/2003JB00252610.1038/35093085>
- Zhou, Q., Hattermann, T., Nøst, O., Biuw, M., Kovacs, K., & Lydersen, C. (2014). Wind-driven spreading of fresh surface water beneath ice shelves in the Eastern Weddell Sea. *Journal of Geophysical Research: Oceans*, 119(6), 3818–3833. <https://doi.org/10.1002/2013JC009556>